Geosci. Model Dev., 19, 10551–10569, 2026
https://doi.org/10.5194/gmd-19-10551-2026
© Author(s) 2026. This work is distributed under
the Creative Commons Attribution 4.0 License.

Geoscientific Model Development
Open Access
EGU

Earth system modelling of mercury using CESM2 – Part 3: Oceanic model POP2/Hg v1.0

Mao Mao[1,2], Yujuan Wang[3], Peng Zhang[4], Ling Li[2], Shaojian Huang[1], Chen Zhou[1], and Yanxu Zhang[2]

[1]School of Atmospheric Science, Nanjing University, Nanjing, 210003, China
[2]Earth & Environmental Sciences, Tulane University, New Orleans, Louisiana 70118, United States
[3]School of Environmental Science and Engineering, Nanjing University of Information Science and Technology, Nanjing, Jiangsu, 210044, China
[4]School of Environment, Hangzhou Institute for Advanced Study, University of Chinese Academy of Sciences, Hangzhou, 310024, China

Correspondence: Yanxu Zhang (yzhang127@tulane.edu)

Received: 9 August 2025 – Discussion started: 15 December 2025
Revised: 5 September 2026 – Accepted: 26 October 2026 – Published: 6 November 2026

Abstract. Mercury (Hg) is a globally distributed toxicant with complex cycling in the ocean, involving redox reactions, air–sea exchange, and microbial methylation. We present POP2/Hg v1.0, a new global ocean mercury model developed within the ocean component of CESM2 (POP2) and coupled to the Marine Biogeochemistry Library (MARBL). POP2/Hg v1.0 simulates dissolved elemental Hg (Hg^0), oxidized Hg (Hg^{II}), particulate-bound Hg (Hg^P), and methylmercury (MeHg = MMHg + DMHg), linking their transformation to ecosystem processes and dynamics of particulate organic carbon (POC). The model captures observed large-scale features of marine Hg. Surface Hg^0 concentrations range from 0.01 to 0.12 pmol L^{-1} (pM, 1 pM = 10^{-12} mol L^{-1}) and are elevated in tropical and subtropical oceans due to strong photoreduction and limited evasion. Subsurface Hg^0 maxima emerge in upwelling zones, reflecting remineralization-driven Hg^{II} reduction. Surface Hg^{II} concentrations peak in regions of high atmospheric deposition and productivity and rise at depth in oxygen-deficient zones. Hg^P is closely associated with high POC and Hg^{II} levels in the surface ocean but attenuates rapidly with depth due to remineralization. MeHg accumulates in the subsurface and deep sea, broadly consistent with observations. Total Hg (Hg^T) at surface generally falls within the range of open-ocean observations, with values of 0.1–1.0 pM across most regions and localized concentrations exceeding 1.2 pM. The biological pump strongly shapes vertical Hg transport. Above 1000 m, soft POC carries 98.55 % of Hg^P flux, driving export and remineralization. Below 1000 m, hard POC becomes relatively more important and accounts for 43.94 % of the integrated Hg^P flux reaching seafloor cells, locally contributing up to over 99 %, although the total flux is small (16.86 Mg yr^{-1}). Sensitivity tests show that altering redox rates significantly affects the vertical distribution of Hg transformations. Reduced surface reduction and oxidation rates increase Hg^0 concentrations in the upper ocean, decrease Hg^{II} concentrations, and weaken seasonal variability. By embedding mercury chemistry into a biogeochemical and physical ocean model which can be potentially fully coupled, POP2/Hg v1.0 offers a process-resolving platform for assessing mercury cycling and its response to environmental change. It enables future integrated Earth system simulations and provides a foundation for simulating marine mercury under future climate and policy scenarios.

1 Introduction

Hg is a toxic heavy metal with long-range transport potential in the atmosphere. As a persistent pollutant, it can migrate and cycle through the atmosphere, ocean, soil, sea ice, and biota, undergoing complex environmental transformations. Among these reservoirs, the ocean contains over 50 times the Hg of the atmosphere (Mason et al., 1994), acting as both a major sink and a re-emission source, and therefore plays a central role in the global mercury cycle. The formation of MeHg, one of the most toxic organic mercury compounds,

poses a critical risk to global human health. It is estimated that the marine food web is the primary pathway for MeHg bioaccumulation, leading to approximately 9.23–10.07 million IQ point losses globally and 29 000–61 800 fatal heart attacks per year (Zhang et al., 2021; Chen et al., 2025). Therefore, understanding mercury cycling in the ocean is of great significance.

The most important source of mercury to the global ocean is the atmosphere, where the gaseous Hg^0 is oxidized via homogeneous or heterogeneous reactions to Hg^{II} that is subsequently deposited into the ocean through dry and wet deposition processes. Riverine input is one of the sources of mercury to the ocean. Mercury originating from land erosion and wastewater discharge is transported via rivers into marine environments. In addition, sediment release and hydrothermal vents also contribute to oceanic mercury inputs. Within the ocean, a portion of Hg^{II} binds to suspended organic-rich particles, sinking under gravity and delivering mercury to the deep ocean. Another portion undergoes microbial methylation to form MeHg, part of which is taken up by marine plankton, entering the food web, and bioaccumulates in higher trophic-level organisms. Upon death, these organisms release Hg either back into the water column or into sediments. In deep, oxygen-deficient waters, mercury reacts with sulfide to form insoluble mercury sulfide (HgS), which settles stably in sediments. As such, deep-sea sediments act as a long-term reservoir for mercury, effectively removing it from active cycling.

Numerical models have been developed to simulate the ocean mercury cycling and its associated processes, but they remain relatively underdeveloped. Early efforts relied on box models (e.g., Sunderland and Mason, 2007), which provided global mass balance estimates but lacked spatial resolution and representation of biogeochemical processes. Two-dimensional slab models (Soerensen et al., 2010) introduced limited vertical structure but neglected horizontal transport and ocean circulation. The emergence of three-dimensional models improved spatial realism, but most current implementations still face significant limitations. Some models operate in an offline mode, meaning they do not simulate ocean physics in real time but instead rely on precomputed ocean state data. Additionally, the spatial resolution of many models is fixed, limiting their adaptability to different scales or regions. Furthermore, many ocean mercury models are difficult to couple with other Earth system components. For example, the OFFTRAC model (Zhang et al., 2014a) is one of the earliest global 3-D ocean mercury models. It lacks MeHg or DMHg species and does not include any dynamic marine ecosystem. The MITgcm-Hg model (Zhang et al., 2020) incorporates ecological variables from the Darwin ecosystem model. However, the coupling with the ecosystem model is performed offline, based on monthly climatological outputs, and does not allow Hg chemistry to respond online to time-evolving ecosystem fields. The model also does not natively support coupling with atmospheric or land surface components, limiting its integration into fully interactive Earth system frameworks. The MERCY v2.0 model (Bieser et al., 2023) provides detailed online coupling between mercury chemistry and a biogeochemical framework, including a plankton food web and particle transport, but it has focused on semi-enclosed seas such as the North and Baltic Seas. It also does not currently include a dynamic sea–ice module and is not coupled to large-scale ocean–atmosphere systems.

The Community Earth System Model version 2 (CESM2) is one of the most advanced global climate modelling frameworks available and provides a promising platform for fully coupled Earth system simulations. In this study, we develop a new global ocean mercury module (POP2/Hg) within CESM2, which simulates key processes such as air–sea exchange, particle partitioning, redox reactions, methylation and demethylation, and mercury transport via the biological pump process. One major advantage is that POP2 is coupled to the Marine Biogeochemistry Library (MARBL), which enables interactive simulation of ecosystem processes, including particulate organic carbon (POC) production and remineralization. MARBL incorporates an online biological pump with separate soft and hard POC pools and simulates sinking particulate organic matter with ballast parameterizations that reflect mineral dust and biogenic material. This improves the representation of particle density, sinking dynamics, and regional variability in carbon transfer efficiency, yielding more realistic POC fluxes from the surface to the mesopelagic ocean (Long et al., 2021). Furthermore, CESM2 already includes dedicated mercury modules for other components, such as CAM6-Chem/Hg for the atmosphere (Zhang and Zhang, 2022), CLM-Hg for terrestrial processes (Yuan et al., 2023), and MOSART-Hg for riverine transport (Peng et al., 2025). This establishes a strong foundation for future full Earth system modelling of mercury, enabling integrated simulations from atmospheric emissions to land erosion, river delivery, and oceanic biogeochemistry.

2 Model description

2.1 Physical Ocean Tracer Model Description

We use the Parallel Ocean Program version 2 (POP2), the ocean component of CESM2, to simulate the global transport and transformation of Hg under present-day conditions. Tracer advection is computed using a third-order upwind-biased scheme, with an optional monotonic flux limiter to minimize numerical dispersion and ensure non-negative concentrations. Vertical mixing is represented using the K-profile parameterization (KPP) scheme, which computes vertical diffusivity and viscosity in the surface boundary layer based on local shear, stratification, and wind forcing. The model is configured on a tripolar curvilinear B-grid, with the North Pole displaced over Greenland to avoid coordinate singularities. It employs 60 vertical z-levels, with enhanced res-

olution in the upper ocean (∼ 10 m layer thickness) to resolve the mixed layer and thermocline structure. Layer thickness increases with depth to approximately 250 m in the abyss, allowing realistic simulation of both upper-ocean processes and deep-ocean tracer transport (Smith et al., 2010). POP2 has previously been used to simulate inert ocean tracers such as CFC-11, CFC-12, and SF_6, which have been widely applied in evaluating large-scale ventilation and circulation patterns (Dutay et al., 2002). Building on this established framework, we extend POP2 to simulate reactive mercury species by incorporating air–sea exchange, redox reactions, and internal oceanic transformations associated with particulate interactions.

For the development of the mercury module, we introduce five passive tracers, Hg^0, Hg^{II}, two forms of MeHg, monomethylmercury (MMHg) and dimethylmercury (DMHg), and particulate-bound mercury (Hg^P) (Fig. 1). We also consider the various processes of its biogeochemical cycle (see Sect. 2.3). For initial development and spin-up, we use the G "Compset" with the T62_g37 grid configuration, which couples an active ocean and sea ice model with prescribed atmosphere and land components. This setup provides a nominal horizontal resolution of approximately 3°. Marine biogeochemistry is enabled through the default MARBL configuration included in CESM2.1.3. All build settings and source files for this configuration are archived in the Zenodo repository associated with this paper.

2.2 Biogeochemistry: MARBL ecosystem and organic carbon cycling

Marine biogeochemical processes in POP2/Hg v1.0 are simulated using the Marine Biogeochemistry Library (MARBL), a modular component of CESM2 that resolves coupled cycles of carbon, nutrients, plankton ecology, and oxygen dynamics. In the configuration used here, the ecosystem is represented using three phytoplankton functional types, which are small phytoplankton, diatoms, and diazotrophs, and one zooplankton grazer. Each phytoplankton type exhibits distinct physiological traits and nutrient requirements. Small phytoplankton dominate in oligotrophic gyres, diatoms require silicate and are prevalent in upwelling and high-latitude regions, while diazotrophs fix atmospheric nitrogen and are restricted to warm, low-nitrate waters. Zooplankton graze on all three phytoplankton types and recycle nutrients through excretion and respiration. MARBL explicitly simulates cycles of macronutrients (nitrate, phosphate, silicate), iron, oxygen, dissolved inorganic carbon (DIC), alkalinity, and both dissolved and particulate organic matter (DOC, POC). Biogeochemical rates such as photosynthesis, nutrient uptake, remineralization, and particle sinking are computed prognostically at every time step, accounting for ambient light, temperature, nutrient concentrations, and ecological stoichiometry. Remineralization of organic matter releases nutrients and dissolved constituents (e.g., Hg^{II}) back into the water column, strongly modulating vertical tracer profiles (Moore et al., 2001, 2004; Long et al., 2021).

As shown in Fig. 2, at 5 m depth, the carbon pool of small phytoplankton and zooplankton are widely distributed in low-latitude regions, particularly in oligotrophic gyres and equatorial zones. Diatoms are concentrated in high-latitude areas and eastern boundary upwelling systems (e.g., off Peru and California), reflecting their preference for nutrient-rich conditions. Diazotrophs are abundant in tropical and subtropical regions (Long et al., 2021). At 95 m depth, the concentrations of all biological components decline significantly, consistent with light and nutrient limitation below the euphotic zone. However, POC maintains higher concentrations at 95 m in coastal upwelling zones, indicating active export of organic material and a strong biological pump (Long et al., 2021).

Organic carbon is partitioned into a "soft" POC pool – composed of rapidly sinking detritus that remineralizes over a few hundred meters – and a "hard" or ballasted POC pool with much longer remineralization length scales (∼ 40 000 m), allowing for deep ocean export. These two POC classes are critical for linking ecological production to elemental cycling and are used in our model to drive particle-associated mercury transport (see Sect. 2.3.4). The total POC flux is highest in regions of elevated primary productivity and intense upwelling, such as the eastern equatorial Pacific, northern Indian Ocean, and Arabian Sea, where values exceed 0.1 mol C m^{-2} yr^{-1}.

Below 2000 m, the behaviors of soft and hard POC diverge markedly. Soft POC flux becomes nearly negligible across the global ocean at 2889 m (Fig. 4a), due to rapid remineralization in the upper mesopelagic. In contrast, hard POC retains fluxes even at 2889 m (Fig. 4b) and in the deepest layer (Fig. 4d). At the sea floor, hard POC becomes the main source of total POC flux (up to 99.96 % maximum and an average of 79.21 % in fraction).

The vertical distribution of the organic carbon remineralization rate shows distinct patterns (Fig. 5). At the surface (5 m), Fremin is generally low, as organic matter production exceeds immediate degradation. At 95 m, remineralization peaks in the North Pacific, North Atlantic, Arabian Sea, and eastern equatorial Pacific, coinciding with high POC export. These zones represent areas of high productivity and efficient particle flux attenuation. In contrast, Fremin values in the deeper zone are nearly zero, indicating that most organic matter is remineralized in the upper 200–300 m.

2.3 Hg Biogeochemistry in the Ocean

2.3.1 Mercury Chemical Reactions

The primary chemical reactions of mercury species included in the model are listed in Table 1. These reactions include photochemical and biogeochemical processes of Hg^0, Hg^{II}, MMHg and DMHg. Reaction mechanism and kinetic param-

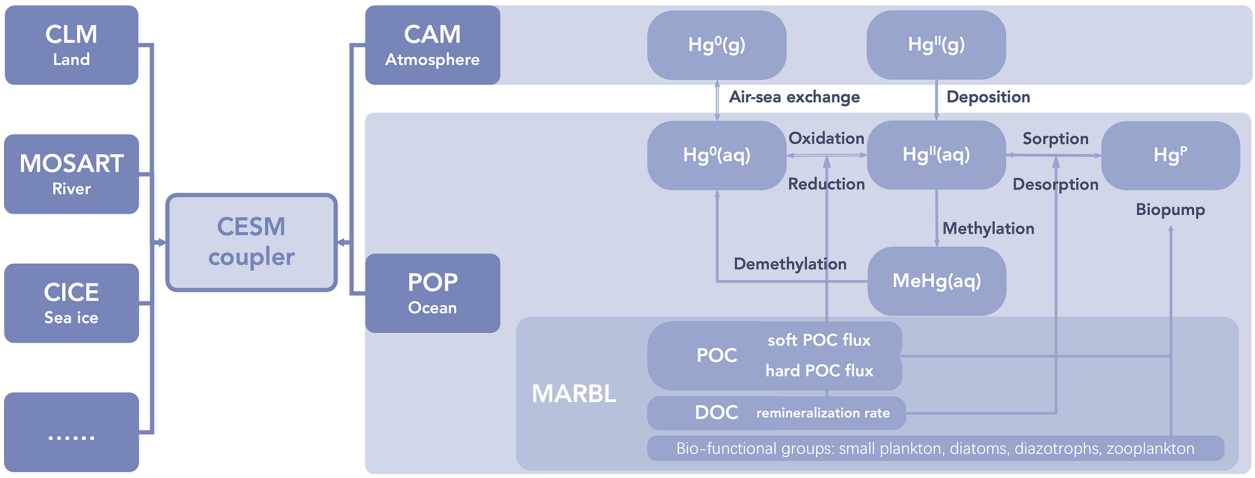


Figure 1. The POP2/Hg v1.0 model framework based on CESM2.

eters adopted from Zhang et al. (2020) comprise a combination of light-driven and biologically mediated conversions. Methylation converts inorganic mercury (mostly Hg^{II}) to the biologically toxic and bio-accumulative form of MMHg and is a key process in the marine Hg cycle. Demethylation, both photochemical and microbial, serves as a counterbalance by converting MMHg back to Hg^0 or Hg^{II}, modulating its concentration and ecological risk. The methylation-demethylation dynamics are tightly coupled to the marine carbon cycle and microbial remineralization pathways.

To couple these transformations to the simulated environment, the light-dependent reaction rates are scaled by the layer-mean shortwave irradiance I ($W\,m^{-2}$), calculated from the surface shortwave radiation after vertical attenuation by seawater, dissolved organic carbon, and the phytoplankton-biomass proxy represented by the summed small-phytoplankton, diatom, and diazotroph carbon tracers. In Table 1, $h\nu$ denotes photon absorption in the photochemical reactions. The organic carbon remineralization rate OCRR is the sum of DOC, refractory DOC, and particulate-organic-carbon remineralization routed to DIC and refractory DOC, expressed in $mmol\,C\,m^{-3}\,d^{-1}$. T_k denotes potential temperature in kelvin.

All numerical base-rate parameters listed in Table 1 were adopted from Zhang et al. (2020). All expressions in the right-hand column yield first-order rate coefficients in s^{-1}, f_{red} is dimensionless and is set to 0.4.

2.3.2 Air–Sea Gas Exchange of Hg^0 and DMHg

The ocean-atmosphere exchange of Hg^0 and DMHg is modelled based on the concentration gradient across the air-sea interface, modulated by solubility (Henry's law constant), the Schmidt number, and sea ice coverage. The net flux direction, either evasion or deposition, is governed by the surface saturation ratio of dissolved Hg species relative to atmospheric concentrations.

The gas transfer velocity PV, also referred to as the piston velocity, is derived from the reference CO_2 transfer velocity and corrected for the sea–ice fraction and the Schmidt number of the target species:

$$\mathrm{PV} = (1 - f_{\mathrm{ice}}) \cdot \mathrm{PV}_{\mathrm{CO_2}} \cdot \sqrt{\frac{Sc_{\mathrm{CO_2}}}{Sc_{\mathrm{Hg}}}} \tag{1}$$

where f_{ice} is the fraction of sea ice, and Sc_{Hg} and Sc_{CO_2} are the Schmidt numbers of the target mercury species and CO_2, respectively. The Schmidt numbers for Hg^0 and DMHg are calculated following Soerensen et al. (2010) and Black et al. (2009), accounting for dependencies on sea surface temperature (SST) and salinity (SSS):

$$Sc_{\mathrm{Hg0}} = \frac{\nu}{D_{\mathrm{Hg0}}},\ Sc_{\mathrm{DMHg}} = \frac{\nu}{D_{\mathrm{DMHg}}} \tag{2}$$

where ν is the kinematic viscosity of seawater, and D is the diffusivity.

With the gas transfer velocity defined, the net air–sea exchange flux F for each gaseous mercury species is then calculated as:

$$F = \mathrm{PV} \cdot (C_{\mathrm{sat}} - C_{\mathrm{surf}}) \tag{3}$$

where PV is the gas transfer velocity (corrected for Schmidt number), C_{surf} is the surface concentration, and C_{sat} is the equilibrium concentration determined by Henry's law:

$$C_{\mathrm{sat}} = \frac{C_{\mathrm{air}}}{H} \tag{4}$$

2.3.3 Sorption of Hg^{II} onto particles

The reversible partitioning of Hg^{II} onto suspended particles is an important process controlling the geochemical species,

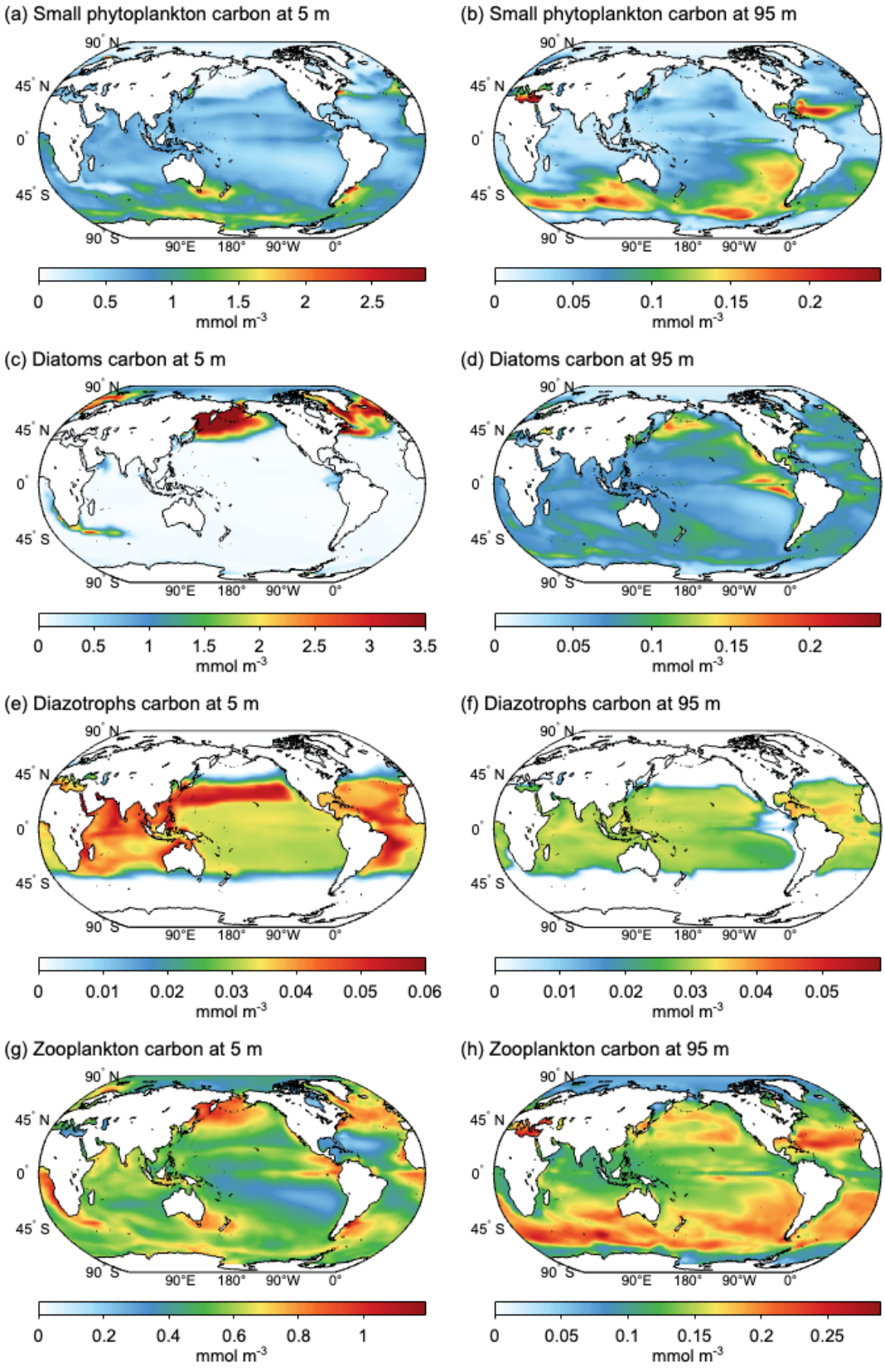


Figure 2. Surface (5 m) and subsurface (95 m) living biomass carbon concentrations simulated by MARBL, units: mmol C m^{-3}.

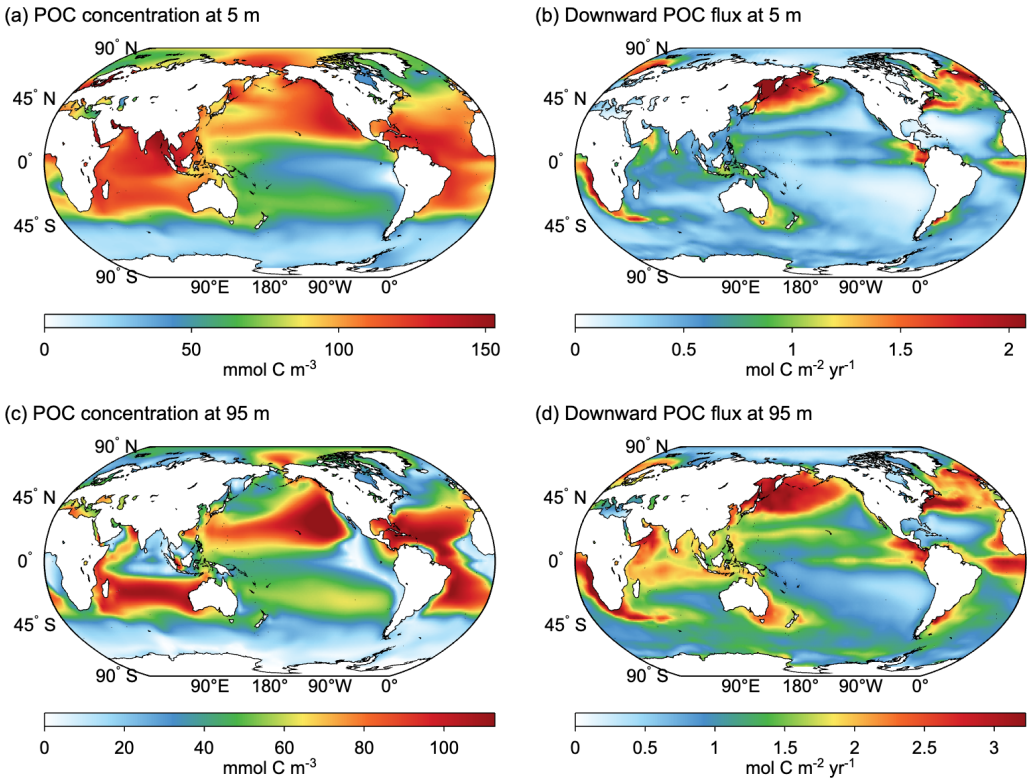


Figure 3. Global maps of total concentration of POC (units: mmol C m^{-3}) and total downward POC flux (units: mol C m^{-2} yr^{-1}) at **(a–b)** 5 m and **(c–d)** 95 m.

Table 1. Kinetic parameters for mercury transformation reactions in the POP2/Hg v1.0 Model.

	Reactions	Reaction rate constant parameters
(R1)	$Hg^0 + h\nu \rightarrow Hg^{II}$	$4.70 \times 10^{-6} I$
(R2)	$Hg^0 \rightarrow Hg^{II}$	$1.30 \times 10^{-9} I + 1.44 \times 10^{-9}$
(R3)	$Hg^{II} + h\nu \rightarrow Hg^0$	$1.56 \times 10^{-6} f_{red} I$
(R4)	$Hg^{II} \rightarrow Hg^0$	2.48×10^{-7} OCRR
(R5)	$Hg^0 \rightarrow Hg^{II}$	9.9×10^{-7} OCRR
(R6)	$Hg^{II} \rightarrow$ MMHg	4.4×10^{-7} OCRR
(R7)	MMHg$\rightarrow Hg^0$	$1.13 \times 10^{-8} \exp\left[5457\left(\frac{1}{293.15} - \frac{1}{T_k}\right)\right]$
(R8)	MMHg $+h\nu \rightarrow Hg^{II}$	$8.0 \times 10^{-8} I$
(R9)	MMHg $\rightarrow$ DMHg	9.3×10^{-9}
(R10)	DMHg $+h\nu \rightarrow$ MMHg	$3.76 \times 10^{-9} I + 1.85 \times 10^{-8}$

transport, and bioavailability of the element in the ocean. Organic-rich particles, such as detritus, biogenic material (e.g., plankton), or mineral clays, are also able to bind Hg^{II}. This particulate-bound mercury (Hg^P) can then undergo gravitational settling, promoting the vertical transport and potential removal from the surface ocean. In the model, we represent this process through an instantaneous equilibrium partitioning between dissolved Hg^{II} and particulate-bound Hg^P, following a linear partitioning assumption (Morel et al., 1998):

$$\frac{Hg^P}{Hg^{II}_{aq}} = \frac{k_d}{f_{oc}}([POC] + [C_{bio}]) \quad (5)$$

where k_d is the partition coefficient and f_{oc} is the organic carbon fraction of suspended particles (assumed to be 10 % following Strode et al., 2010), [POC] is the concentration of non-living detrital particulate organic carbon, and $[C_{bio}]$ is the living particulate biomass carbon concentration available for Hg^{II} partitioning. In the simulated configuration,

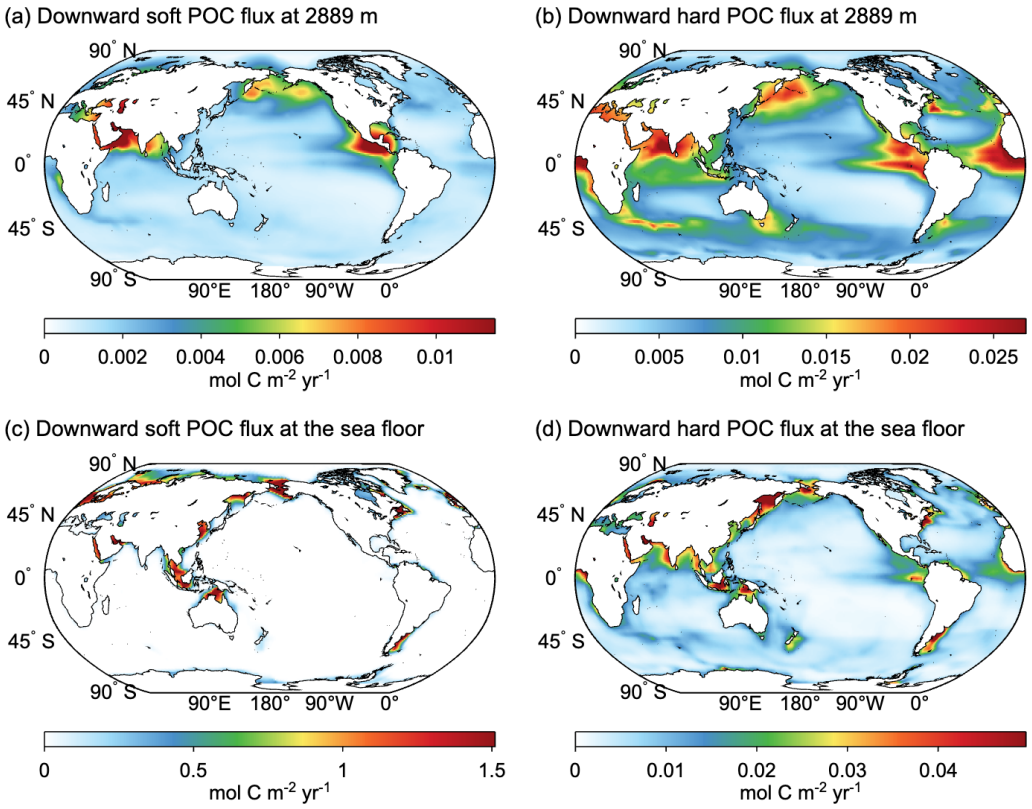


Figure 4. Depth-separated downward flux of soft and hard POC at **(a)** and **(b)** 2889 m, and **(c)** and **(d)** the deepest layer of the sea, respectively.

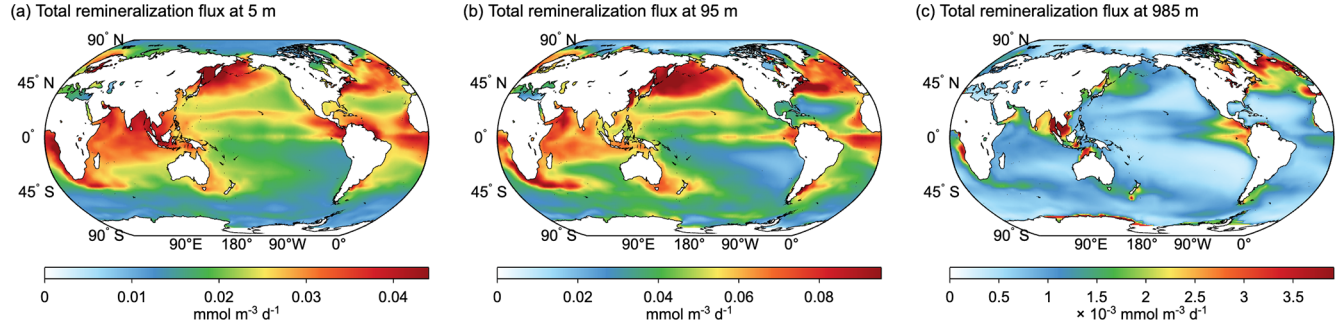


Figure 5. Vertical distribution of organic carbon remineralization rate (Fremin) at **(a)** 5 m, **(b)** 95 m, and **(c)** 985 m. Units: mmol C m^{-3} d^{-1}.

$k_d = 10^{5.15}$ L kg^{-1}, $[C_{bio}]$ includes the carbon biomass concentrations of small phytoplankton, diatoms, diazotrophs, and zooplankton.

Unlike prior studies that applied offline POC fields (e.g., Zhang et al., 2020), we dynamically calculate this partitioning using the vertically resolved and time-evolving POC fields from MARBL.

2.3.4 Biological Pump Transport of Particulate Hg

Hg^P is simulated in our model by coupling it to the vertical transport of POC as diagnosed by the MARBL ecosystem module. MARBL resolves two classes of POC with distinct biogeochemical behaviors: soft POC, which is labile and sinks rapidly but is typically remineralized within the upper hundreds of meters; and hard POC, which is associated with ballasted particles and exhibits slow degradation over length scales up to ∼ 40 000 m, enabling long-distance transport into the deep ocean.

We assume that inorganic Hg^{II} partitions onto organic particles via a fixed distribution coefficient (see Sect. 2.3.3), and that once adsorbed, the resulting Hg^P is vertically exported alongside the particles. The effective sinking rate of Hg^P is dynamically computed using the ratio of total particulate flux

to total particulate concentration:

$$v_{\text{sink}} = \frac{F_{\text{POC}} + F_{\text{bioC}}}{[\text{POC}] + [C_{\text{bio}}]} \quad (6)$$

Here, F_{POC} represents the sinking flux of non-living detrital POC, while F_{bioC} represents the sinking flux of living particulate biomass, calculated as

$$F_{\text{bioC}} = \sum_p w_p C_p \quad (7)$$

To adapt this formulation to the living-particle groups represented in the present MARBL configuration, diatoms and diazotrophs are assigned settling velocities of $0.5\,\text{m}\,\text{d}^{-1}$, whereas small phytoplankton and zooplankton are assigned zero settling velocity, following Zhang et al. (2020).

The vertical flux of Hg^{P} is then given by:

$$f_{\text{out}} = v_{\text{sink}} \cdot \text{Hg}^{\text{P}} \quad (8)$$

A maximum velocity of $0.5\,\text{m}\,\text{d}^{-1}$ is imposed to guarantee physical consistency and to prevent excessive export in oligotrophic regimes.

To distinguish the Hg^{P} transport associated with the two MARBL POC classes, we additionally diagnose soft- and hard-POC associated Hg^{P} sinking fluxes by replacing F_{POC} in Eq. (6) with $F_{\text{POC,soft}}$ and $F_{\text{POC,hard}}$ respectively.

This formulation allows the sinking rate of Hg^{P} to vary dynamically in space and time, responding to ecological processes such as phytoplankton blooms, detritus production, and aggregation. As particles sink and undergo remineralization or grazing, the associated Hg^{P} is removed from the water column, either lost to sedimentation or recycled via desorption and re-equilibration with the dissolved phase. In the simulations analyzed here, Hg^{P} flux leaving the deepest wet grid cell is treated as a terminal seafloor export from the ocean water column. MARBL provides seafloor POC burial diagnostics, and the model architecture retains an optional interface for separating permanent burial from benthic recycling, however, this interface was not activated in the present simulations.

2.4 Initial Conditions, Atmospheric Forcing, and Evaluation Dataset

For the simulations in this study, the five ocean Hg tracers were initialized using externally prescribed three-dimensional fields prepared for the MITgcm-Hg configuration described by Zhang et al. (2020). These fields were interpolated onto the POP2 grid and used to initialize the corresponding POP2/Hg tracers. Starting from the prescribed initial fields, POP2/Hg was integrated for 10 years. To assess the influence of integration length, an otherwise identical baseline simulation was extended to 20 years. The vertically integrated Hg^{T} inventories within the upper 500 m differed by less than 1 % between the 10- and 20-year simulations, indicating that extending the integration had only a minor effect on the upper-ocean Hg^{T} results examined in this study. As the present study focuses primarily on the upper ocean, the 10-year simulation was used for model evaluation and process analysis. Longer integrations would be required to investigate changes in the deeper ocean in response to ocean circulation and biogeochemical processes.

The model uses atmospheric Hg^0 concentration and Hg^{II} deposition prescribed from the CAM6-Chem/Hg model output (Zhang and Zhang, 2022) as atmospheric forcing input (Fig. 6). Hg^0 forcing is strongest in the western Pacific, broadly reflecting the influence of nearby anthropogenic source regions. Hg^{II} deposition dominates in the intertropical convergence zone (ITCZ), North Indian Ocean, and eastern equatorial Pacific, consistent with wet deposition patterns driven by deep convection. The current model does not yet include riverine mercury input and focuses on the development and evaluation of the ocean module. The coupling with riverine inputs and the land component will be incorporated in future work. For DMHg, the atmospheric concentration is held spatially and temporally constant at $4\,\text{pg}\,\text{m}^{-3}$, following Zhang et al. (2020).

The model evaluation utilized a compiled dataset of ocean Hg concentrations provided by Zhang et al. (2020), and air–sea exchange flux collected by Kuss et al. (2011), Soerensen et al. (2013, 2014), Wang et al. (2017), Kalinchuk et al. (2021), and Nerentorp Mastromonaco et al. (2017). These data were used to evaluate model outputs.

3 Results

3.1 Hg^0

The modelled dissolved elemental mercury (Hg^0) concentrations in surface waters typically range from 0.04 to 0.08 pM, accounting for approximately 10 % of Hg^{T} in the upper ocean (Fig. 7a). Localized maxima reaches approximately 0.12 pM, with high concentrations (> 0.10 pM) occurring in the western Pacific warm pool and eastern equatorial Pacific. In contrast, localized low Hg^0 levels (< 30 fM) occur in the North Indian Ocean and Arabian Sea. These patterns are driven by sea surface temperature, solar irradiance, and wind speed: warmer, low-latitude regions with high light availability and low wind speeds favor photoreduction of Hg^{II} and reduced evasion, allowing accumulation of Hg^0 in surface waters.

Figure 7a presents the spatial distribution of modelled surface Hg^0 along with pointwise observations for comparison. The model qualitatively captures the broad enhancement of Hg^0 concentrations in tropical and subtropical regions well, and reproduces the observed order of magnitude at many open-ocean locations, with simulated concentrations generally ranging from 0.04 to 0.08 pM. However, significant discrepancies occur in coastal and estuarine zones such as Southeast Asia and the eastern seaboard of North

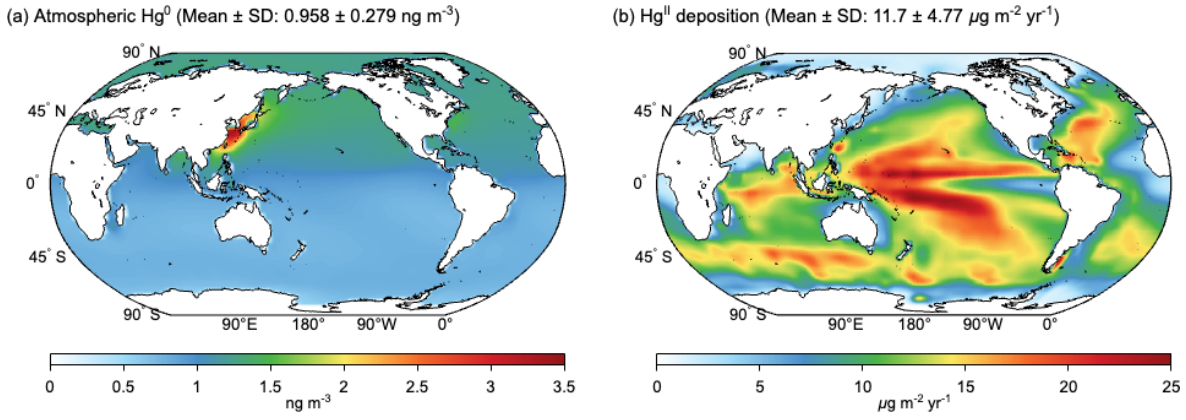


Figure 6. Atmospheric mercury input fields used as model forcing: **(a)** atmospheric Hg^0 concentration, units: ng m^{-3} and **(b)** Hg^{II} deposition, units: μg m^{-2} yr^{-1}.

America, where some of the observed values exceed 0.2 pM, while simulated Hg^0 concentrations generally remain around 0.07 pM. The collocated comparison shows a significant positive spatial association ($r = 0.35$, $p < 0.001$, $n = 381$). Correlations are stronger in the northern and southern subtropics ($r = 0.39$ and 0.53, respectively; both $p < 0.001$), with NMBs of −47.1 % and +62.5 %, respectively. These differences likely result from the lack of riverine Hg input and limited resolution nearshore, which are not yet incorporated in the model. In polar regions, additional discrepancies may arise from the omission of Hg uptake by and release from sea ice during ice formation and melt.

At 95 m depth, the modelled Hg^0 concentrations typically range from 0.02 to 0.08 pM, and in some regions exceed surface values, locally reaching up to 0.18 pM in upwelling zones. This increase is particularly evident in upwelling and remineralization zones such as the eastern equatorial Pacific, North Indian Ocean, and the subtropical boundary currents. At this depth, light attenuation limits photoreduction, while remineralization-driven Hg^{II} reduction increases the fraction of Hg^0, combined with weaker air–sea exchange rates that allow greater retention of Hg^0. At 985 m depth, the simulated Hg^0 distribution remains strongly influenced by the prescribed initial field, with a spatial correlation of 0.93 between the simulated and initial fields.

3.2 Hg^{II}

The simulated distribution of Hg^{II} reflects the combined influence of atmospheric deposition, redox transformations, and internal cycling. At the sea surface (Fig. 8a), Hg^{II} concentrations range from approximately 0.1 to 0.8 pM, with elevated values in the North Indian Ocean, tropical western Pacific, and parts of the South China Sea. These regions coincide with intense wet and dry deposition of atmospheric Hg^{II} and zones of active photochemical cycling. Extreme values occur in biologically productive or upwelling regions, such as the Bay of Bengal and Southeast Asian marginal seas, where concentrations locally reach up to 2.0 pM.

At 95 m depth (Fig. 8b), Hg^{II} concentrations are markedly enhanced in high-productivity or upwelling regions, including the eastern equatorial Pacific and the Arabian Sea, typically ranging from 0.3 to 0.8 pM. This enhancement is primarily due to the downward export and remineralization of Hg^P, combined with reduced photoreduction efficiency that limits the conversion to Hg^0. In addition, oxygen-deficient zones at this depth promote the persistence of divalent mercury, making them key sources of microbial methylation. At 985 m depth (Fig. 8c), Hg^{II} becomes the largest dissolved mercury species. High concentrations are observed in the North Pacific and equatorial Atlantic, approaching 1.5 pM. Similar to Hg^0, this deep distribution remains partly influenced by the initial field after the 10-year integration.

The simulated Hg^P reflects the combined influences of particulate POC and Hg^{II} in both horizontal and vertical dimensions. At the ocean surface (Fig. 9a), Hg^P concentrations exhibit distinct regional maxima in the northwestern Indian Ocean, equatorial Atlantic, and northeastern Pacific, particularly in the Bay of Bengal, where values exceed 0.3 pM. Elevated Hg^P concentrations are co-located with regions where both POC levels and Hg^{II} concentrations are relatively high (see Figs. 3a and 8a), promoting enhanced sorption of Hg^{II} onto organic particles.

At 95 m depth (Fig. 9b), Hg^P concentrations get lower, with the highest values (exceeding 0.07 pM) persisting in subsurface convergence and export regions such as the western Pacific and eastern equatorial Atlantic. The influence of POC dominates over that of Hg^{II}, as high Hg^P concentrations closely correspond to regions of elevated POC. At 985 m depth (Fig. 9c), where biological productivity declines sharply, Hg^P concentrations nearly vanish. At this depth, the dominant process becomes remineralization, and nearly all Hg^P is converted back to the dissolved form, with notable residual Hg^P concentrations only persisting in localized re-

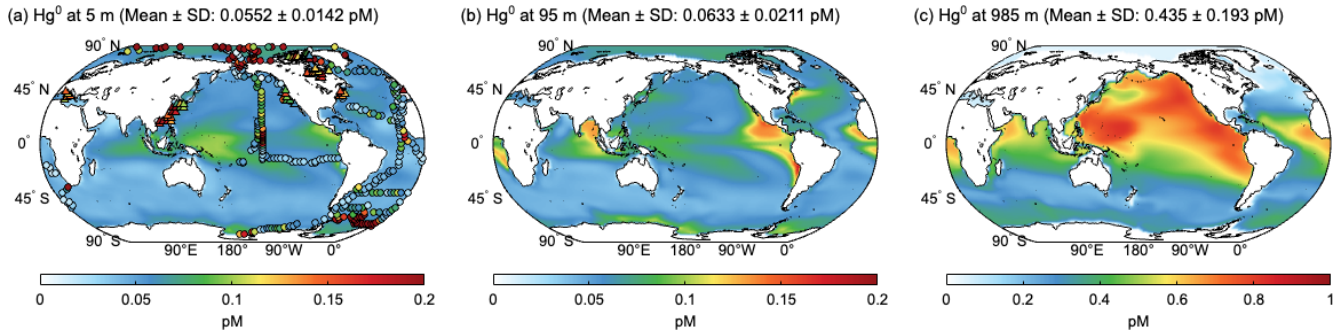


Figure 7. Modelled concentrations of Hg^0 at **(a)** surface (5 m), with scattered observations; **(b)** 95 m; **(c)** 985 m. Units: pM.

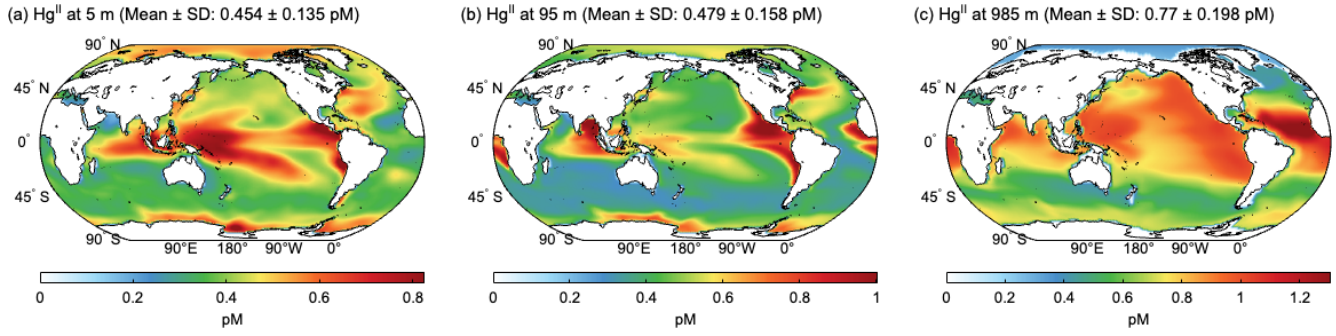


Figure 8. Modelled concentrations of Hg^{II} at **(a)** surface (5 m); **(b)** 95 m; **(c)** 985 m. Units: pM.

gions where POC remains. This vertical attenuation of Hg^P aligns with previous modeling studies (e.g., Sunderland and Mason, 2007; Zhang et al., 2014b).

3.3 MeHg

The simulated distribution of MeHg, including MMHg and DMHg, exhibits pronounced vertical and regional gradients shaped by subsurface methylation, biological productivity, and redox conditions. Across the three evaluated depths, the collocated MeHg comparison gives $r = 0.47$ ($p < 0.001$, $n = 259$), RMSE $= 0.156$ pM, and NMB $= -11.7\,\%$, indicating that the model captures part of the overall spatial variability with a moderate negative bias.

At the surface (Fig. 10a), MeHg concentrations remain generally low across most of the global ocean, typically below 0.05 pM. However, due to strong photo-demethylation and rapid air–sea exchange of volatile DMHg, surface MeHg remains significantly depleted relative to deeper layers. This indicates that surface MeHg is tightly regulated by photochemical loss and air–sea fluxes (Soerensen et al., 2010; Zhang et al., 2020). These open ocean surface patterns correspond with available observations generally ($r = 0.49$, $p < 0.001$, $n = 86$).

At 95 m depth (Fig. 10b), peak MeHg concentrations increase and occur in regions of high productivity or upwelling, such as the eastern tropical Pacific, equatorial Atlantic, and the northern Indian Ocean, with simulated values exceeding 0.12 pM. The model captures part of the observed spatial variability ($r = 0.37$, $p < 0.001$, $n = 78$), matching observed hotspots along the eastern boundary currents (e.g., Peru and California coasts) and lower in open waters, although regional biases remain. In the North Pacific and tropical Atlantic, the available observations and modelled values are generally of the same ranges, but the regional sample sizes are small.

At 985 m (Fig. 10c), the model simulates widespread accumulation of MeHg, with background values around 0.1–0.3 pM, and local maxima exceeding 0.6–0.8 pM in the North Pacific interior. These elevated values are consistent with observations from deep sampling campaigns, especially in the North Pacific Subarctic Gyre and Equatorial Pacific, where deep MeHg concentrations often exceed 0.5 pM. The persistence of MeHg at these depths is likely to be sustained by slow degradation rates and limited transport, allowing accumulation over longer timescales. This pattern is consistent with previous global ocean mercury models (e.g., Wang et al., 2023). When compared with observation, association remains positive ($r = 0.42$, $p < 0.001$, $n = 95$) although the model generally overestimates MeHg. The distribution also remains influenced by the prescribed initial field.

3.4 Hg^T

At the surface (Fig. 11a), simulated Hg^T concentrations generally range from 0.1 to 1.0 pM, with higher values

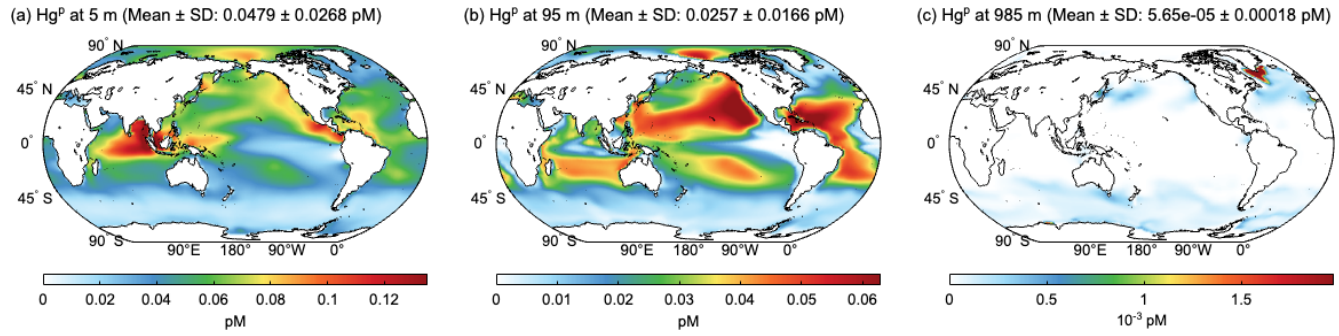


Figure 9. Modelled concentrations of Hg^P at **(a)** 5 m; **(b)** 95 m; **(c)** 985 m. Units: pM.

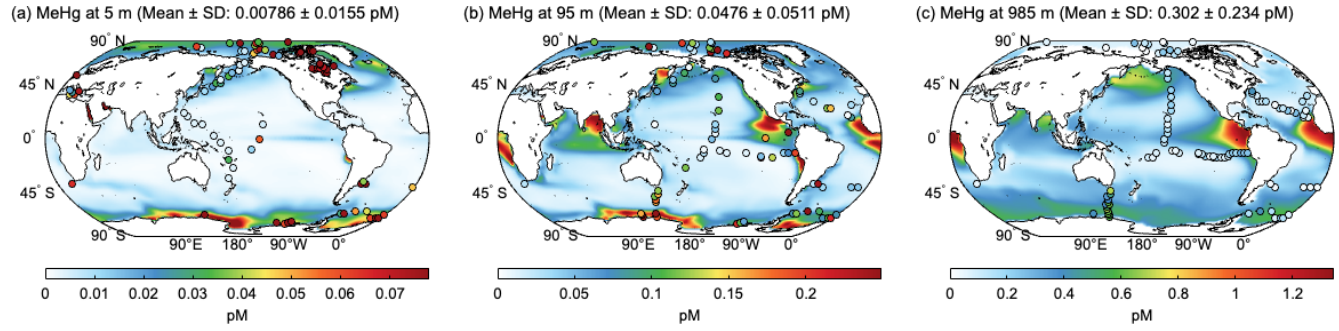


Figure 10. Modelled concentrations of MeHg compared with observations at **(a)** 5 m; **(b)** 95 m; **(c)** 985 m. Units: pM.

(> 1.2 pM) found in the equatorial Pacific, western boundary currents (e.g., Gulf Stream, Kuroshio), and eastern boundary upwelling zones (e.g., off Peru and southwest Africa). The patterns capture part of the broad surface spatial variability, but local agreement remains modest ($r = 0.29$, $p < 0.001$, NMB $= -64.2\,\%$, $n = 140$), indicating a substantial overall underestimate. For example, in the North Atlantic Ocean (excluding coastal regions), observed Hg^T concentrations at the surface range from 0.6 ± 0.2 pM, while the model simulates values around 0.7 ± 0.1 pM. In contrast, the model underestimates Hg^T in some coastal and marginal seas, including Southeast Asia, the Gulf of Mexico, and the western North Atlantic shelf. These mismatches likely arise from the exclusion of riverine Hg inputs and insufficient resolution of shelf and margin dynamics in the current model configuration.

At 95 m depth (Fig. 11b), elevated concentrations persist in eastern boundary regions and extend westward into the tropical Atlantic and Pacific basins. Simulated Hg^T values typically range from 0.4 to 1.4 pM at this depth, showing good agreement with observations ($r = 0.49$, $p = 0.0013$, $n = 41$).

At 985 m, (Fig. 11c), Hg^T shows widespread accumulation. In parts of the Atlantic Ocean and the Southern Ocean, the model tends to overestimate deep Hg^T relative to observations. Because the deep ocean does not fully adjust over the integration period, this mismatch may partly reflect the prescribed initial field.

Across the evaluated Hg species, the collocated comparisons generally show positive model–observation associations and reproduce the observed ranges, although the magnitude and direction of the biases vary among species, regions, and depths. The largest discrepancies occur in coastal regions. The nominal 3° configuration is selected to enable computationally efficient model development, iterative testing, and sensitivity experiments. However, its relatively large grid cells cannot adequately resolve narrow continental shelves, estuarine exchange, coastal currents, or mesoscale eddies. Riverine Hg inputs are also not represented in the present model configuration, partly because their transport and dilution cannot be resolved adequately at this spatial resolution. The resulting underestimation in some coastal and marginal seas is therefore consistent with the current model structure and forcing.

In the open ocean, most Hg observations were collected along ship tracks during individual cruises and represent specific seasons, hydrographic conditions, and short-term meteorological states. In contrast, the model fields represent annual-mean conditions at the global scale. Differences at individual sampling locations can consequently arise from spatial and temporal sampling mismatches. In addition, the model is driven by the atmospheric Hg deposition flux predicted by the CAM6-Chem/Hg model, which simulates an elevated flux in the tropical region due to the inclusion of OH/O_3 oxidation of Hg^0 and the absence of sea salt debromination processes (Zhang and Zhang, 2022). This poten-

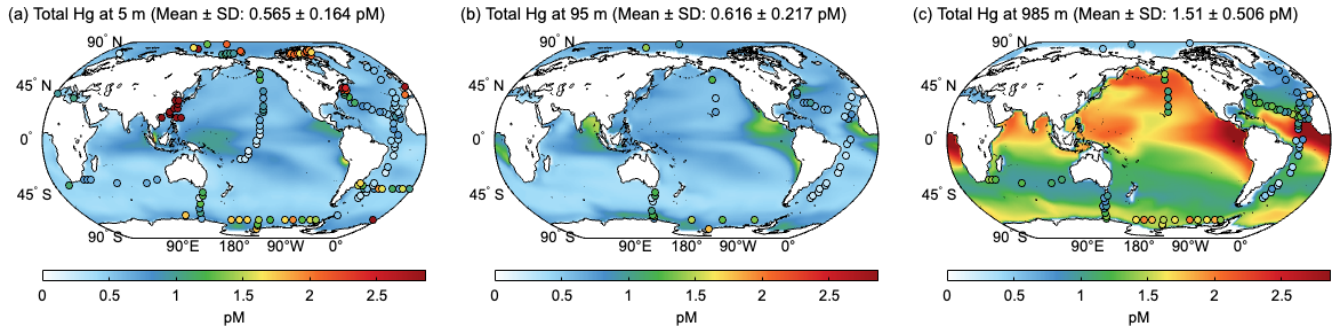


Figure 11. Modelled concentrations of Hg^T compared with observations at **(a)** 5 m, **(b)** 95 m, and **(c)** 985 m. Units: pM.

tial overestimation of atmospheric Hg deposition may bias the simulated oceanic Hg^T concentrations, particularly at lower latitudes. These factors partly explain the greater scatter in comparisons at individual sampling locations. Nevertheless, the simulated fields reproduce the major basin-scale Hg gradients in the available observations. At depth, the continuing influence of the prescribed initial conditions also contributes to the model–observation differences.

4 Mercury Transformation and Vertical Fluxes

4.1 Air–Sea Exchange

The ocean surface acts as the primary interface for the exchange of Hg between the atmosphere and the ocean. Model simulations estimate a global Hg^0 net evasion flux of approximately 4.52×10^3 Mg yr^{-1}. Including DMHg, the simulated total net gaseous Hg evasion is 4.61×10^3 Mg yr^{-1}, comparable to the atmospheric Hg^{II} deposition flux of 4.20×10^3 Mg yr^{-1}, indicating a near balance in global air–sea Hg exchange.

In Fig. 12, net air–sea exchange flux is defined as Hg species come into the sea minus emissions, positive values indicate net input, and negative values indicate net emission. Spatially, Hg^0 evasion is strongest in tropical and subtropical regions, where warm surface waters and high solar radiation enhance photoreduction and lead to Hg^0 supersaturation. Elevated fluxes are also observed in the South Pacific and Indian Ocean. Along the western boundary of the North Atlantic, enhanced evasion is driven by the Gulf Stream's elevated temperatures and wind speeds. The Southern Ocean shows strong evasion as well, attributed to persistent westerlies and high wind forcing.

Table 2 compares selected ocean Hg inventories and net air–sea exchange in POP2/Hg with corresponding estimates for MITgcm-Hg and ICON-MERCY obtained from MCHgMAP model outputs. The MCHgMAP model-comparison framework is described by Dastoor et al. (2025). Net air–sea exchange is defined as positive into the ocean, and negative values therefore indicate net Hg evasion. For POP2/Hg, annual-mean concentrations are integrated over native wet-cell volumes, using the model interfaces at 50.0 and 1041.4 m as the boundaries of the nominal surface, intermediate, and deep-ocean reservoirs. All three models produce comparable surface-ocean inventories and simulate net oceanic Hg evasion. The intermediate-, deep-, and total-ocean POP2/Hg inventories are closer to the MITgcm-Hg estimates, whereas ICON-MERCY produces substantially larger intermediate and deep-ocean inventories. The agreement with MITgcm-Hg is consistent with the use of its Hg initial fields and chemical parameterizations in POP2/Hg and provides a useful consistency check that their implementation within the POP2 circulation and MARBL biogeochemistry preserves the first-order vertical inventory structure. The remaining differences reflect variations in vertical grids, forcing, circulation, ecosystem representation, and diagnostic definitions, and the comparison therefore provides a broad model-to-model benchmark rather than a controlled budget intercomparison.

4.2 Chemical Transformation

Inorganic mercury transformations in the ocean, including redox and methylation reactions, vary with depth, region, and season (Figs. 13–15). Integrated over the surface ocean (0–50 m), gross reduction slightly exceeds gross oxidation in the surface layer, giving a weak net tendency toward Hg^0 formation that is consistent with the simulated Hg^0 evasion. Photoreduction of Hg^{II} is particularly strong at low-latitude regions, with maxima in the equatorial Pacific, North Atlantic gyres, and the Indian Ocean (> 40 µg m^{-3} yr^{-1}), consistent with intense solar irradiance and shallow mixed layers.

At intermediate depths (50–1000 m), the vertically integrated redox budget remains net reducing, with an annual total flux of 1.74×10^3 Mg yr^{-1}. Both oxidation and reduction rates at 95 m (Fig. 13c–d) are roughly one order of magnitude lower than surface values, but oxidation becomes dominant in certain mid-depth waters, notably in the North Atlantic and eastern equatorial Pacific upwelling zones. At 985 m (Fig. 13e–f), redox fluxes further decrease by roughly three orders of magnitude, and a net oxidation trend emerges. Inte-

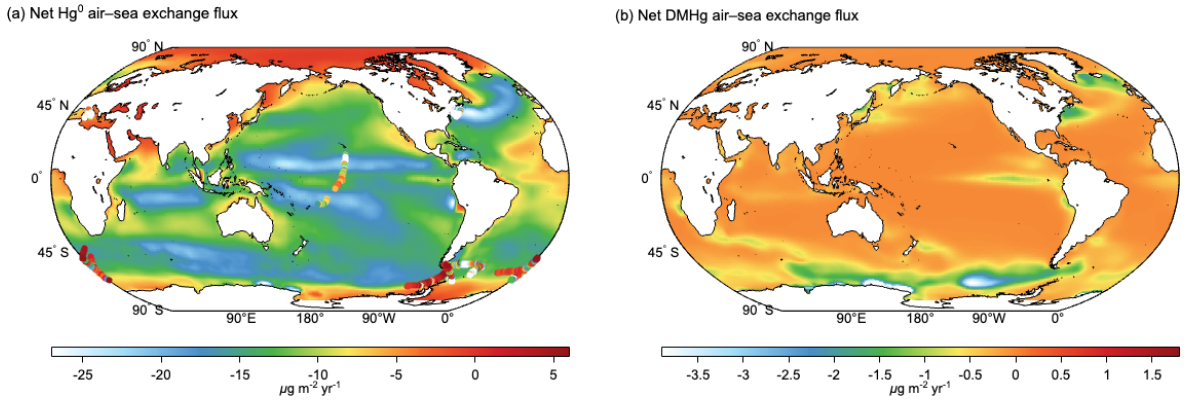


Figure 12. Air-sea exchange flux of Hg^0 (with observations) and DMHg. Units: $\mu g\,m^{-2}\,yr^{-1}$.

Table 2. Comparison of selected ocean Hg inventories and net air–sea exchange in POP2/Hg, MITgcm-Hg, and ICON-MERCY.

Budget	POP2/Hg	MITgcm-Hg	ICON-MERCY
Surface ocean inventory (Gg)	2.03	1.67	1.73
Intermediate ocean inventory (Gg)	82.4	62.1	172
Deep ocean inventory (Gg)	279	263	629
Total ocean inventory (Gg)	364	327	803
Net air–sea exchange ($Mg\,yr^{-1}$)	−4610	−4375	−3536

grated over the deep ocean below 1000 m, the redox budget shows net oxidation of $3.74 \times 10^3\,Mg\,yr^{-1}$, suggesting slow but sustained chemical transformation of Hg^0 to Hg^{II} in deep waters.

The spatial distributions of methylation and demethylation rates are closely linked to the modelled Hg^{II} concentrations and organic matter remineralization patterns (Figs. 3 and 5). Regions of enhanced methylation tend to coincide with strong remineralization zones, particularly at 95 m depth in the eastern tropical Pacific, the northwest Pacific, and the Arabian Sea. Besides, the regeneration of Hg^{II} from sinking organic matter plays a key role in promoting MeHg production. While in surface waters (5 m depth), demethylation dominates, reflecting efficient photochemical and microbial degradation processes under high light conditions.

The corresponding layer-integrated net budgets indicate net demethylation of $1.17 \times 10^3\,Mg\,yr^{-1}$ in surface waters and $2.96 \times 10^3\,Mg\,yr^{-1}$ in the deep ocean. In intermediate waters, annual methylation fluxes are $84.99\,Mg\,yr^{-1}$, and methylation hotspots align with remineralization zones, especially in the eastern tropical Pacific, the northwest Pacific, and the Arabian Sea. These processes are supported by regenerated Hg^{II} from sinking organic matter. However, the relatively coarse horizontal resolution of the model may lead to an underestimation of localized methylation or demethylation hotspots in these regions.

Seasonal variation is pronounced in surface redox fluxes, with higher rates near the beginning and end of the year and a minimum around June (Fig. 15). Methylation and demethylation show less seasonality and remain active throughout the year, especially at depths > 1000 m, where conditions are more stable.

4.3 Biological Pump and Vertical Transport

As shown in Fig. 16, the downward flux of Hg^P associated with soft and hard POC exhibits distinct spatial and vertical patterns, coinciding with the contribution of soft and hard POC fluxes (Figs. 3 and 4). Across the 50 m interface, the total downward Hg^P flux is $5.55 \times 10^2\,Mg\,yr^{-1}$, of which soft- and hard-POC-associated pathways account for 5.49×10^2 and $6.41\,Mg\,yr^{-1}$, respectively. Thus, soft POC dominates upper-ocean Hg^P transport, whereas hard POC contributes only 1.15 % of the total.

Across the 1041 m interface, the downward Hg^P flux decreases by more than three orders of magnitude, reflecting extensive particle remineralization within the intermediate ocean. Although soft POC remains the dominant carrier, the hard-POC-associated contribution increases to approximately 10.0 %.

In contrast, the contribution pattern changes with increasing depth, and hard POC becomes relatively more important than in the upper ocean. Over the upper 1000 m, the vertically integrated diagnostic attributes 98.55 % of the combined soft- and hard-POC-associated Hg^P flux to the soft-POC pathway. Across all seafloor grid cells, the modeled Hg^P export is $16.86\,Mg\,yr^{-1}$. For seafloor cells deeper than 1000 m, the flux-weighted hard-POC-associated contribution

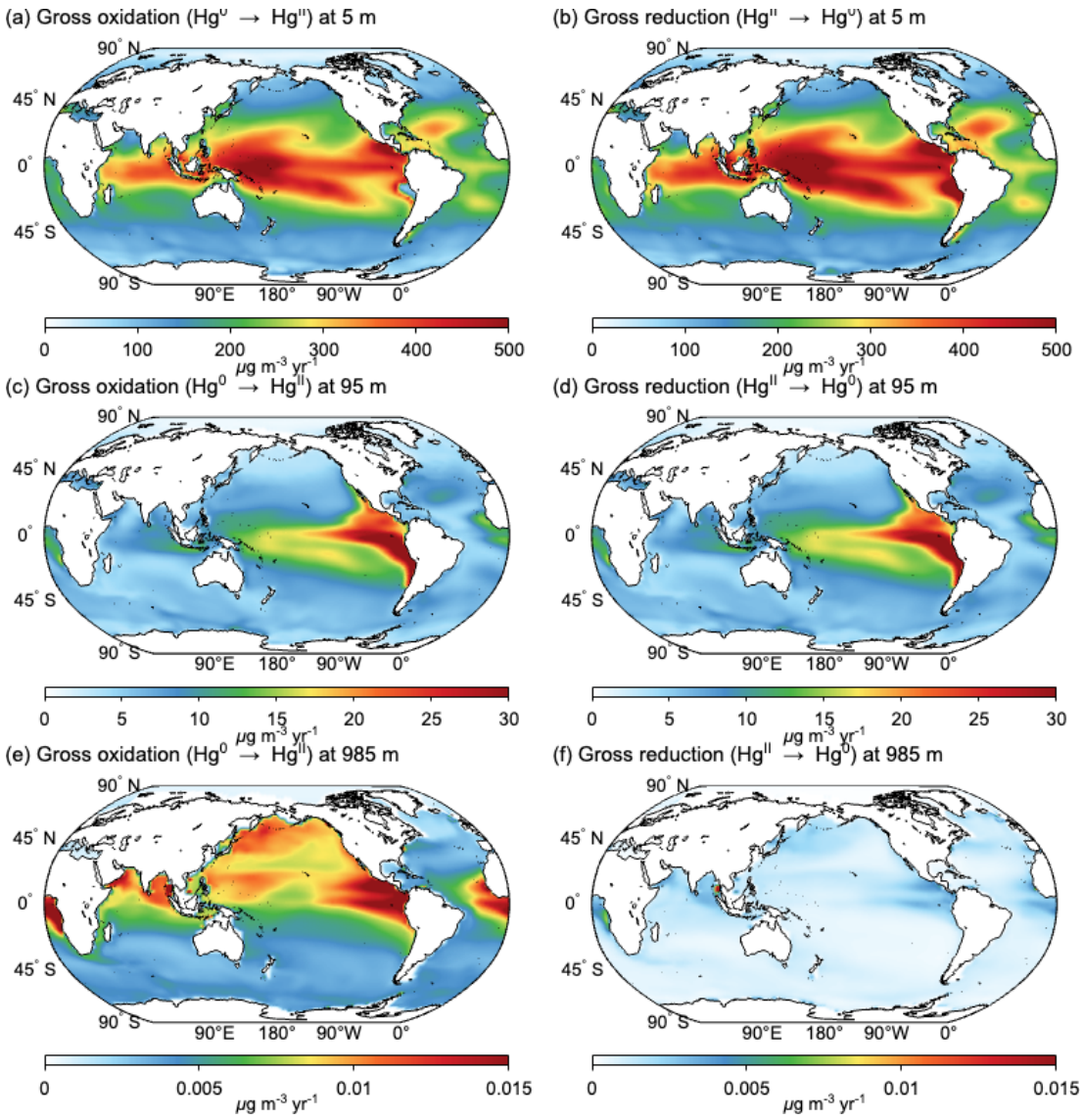


Figure 13. Spatial distribution of annual gross inorganic mercury redox transformations at three depths. **(a, c, e)** Oxidation from Hg^0 to Hg^{II}; **(b, d, f)** Reduction from Hg^{II} to Hg^0. Panels correspond to depths of 5, 95, and 985 m, respectively.

increases to 43.94 % and locally exceeds 99 %. The persistence of hard POC at depth supports its role as an important carrier of Hg^P below 1000 m. However, its impact on deep-ocean Hg^P inventories remains limited due to both the small Hg load and the continued degradation of POC. Overall, the biological pump redistributes mercury vertically via particle-associated transport, with pronounced stratification.

4.4 Sensitivity to redox chemistry

To assess the model's sensitivity to redox rates, we compared a 20-year baseline simulation with a 20-year reduced-rate simulation following Bieser et al. (2023): the light-normalized Hg^0 oxidation coefficient was lowered from 4.7×10^{-6} to 2.4×10^{-7} $m^2\,W^{-1}\,s^{-1}$, and the Hg^{II} photoreduction from 1.6×10^{-6} to 1.0×10^{-8} $m^2\,W^{-1}\,s^{-1}$, while all other parameters remained unchanged.

These changes lead to weaker net reduction at the surface (0–50 m), lowering net redox fluxes from 1.67×10^5 to 8.22×10^3 Mg yr^{-1}. Hg^0 evasion slightly increased from 4.43×10^3 to 4.86×10^3 Mg yr^{-1}. The most pronounced changes occur in the surface ocean. At 5 m, Hg^{II} concentrations decrease substantially, while Hg^0 concentrations approximately double. This leads to a 10 % increase in the air–sea evasion flux of elemental mercury. Meanwhile, total mercury concentrations in the surface ocean decline markedly, although deep-ocean total mercury remains largely consistent with the baseline simulation. In the mid-depth ocean, net reduction increased from 1.53×10^3 to 3.62×10^3 Mg yr^{-1}.

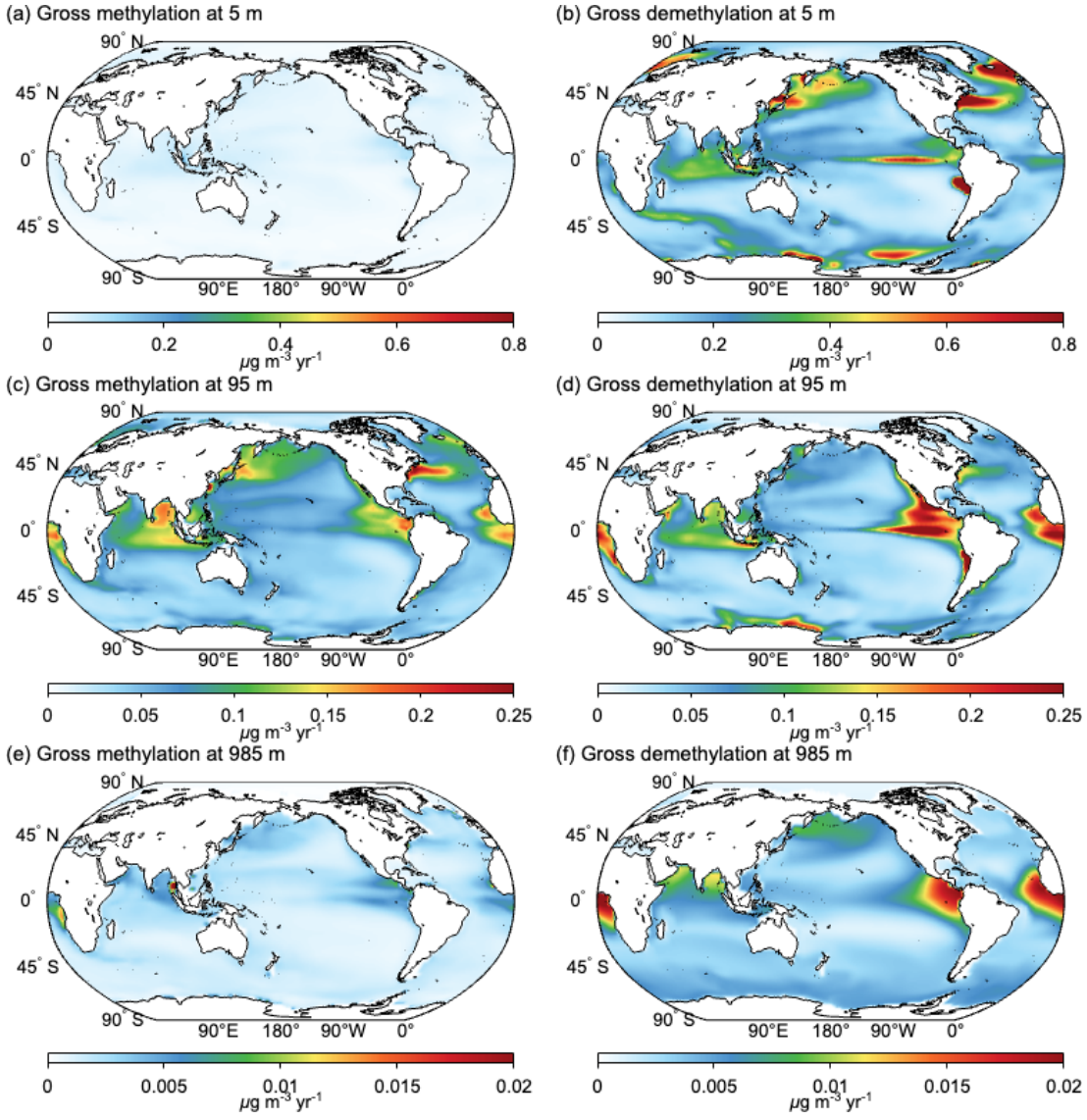


Figure 14. Spatial distribution of annual gross **(a, c, e)** methylation and **(b, d, f)** demethylation of mercury species across 5, 95, and 985 m, respectively.

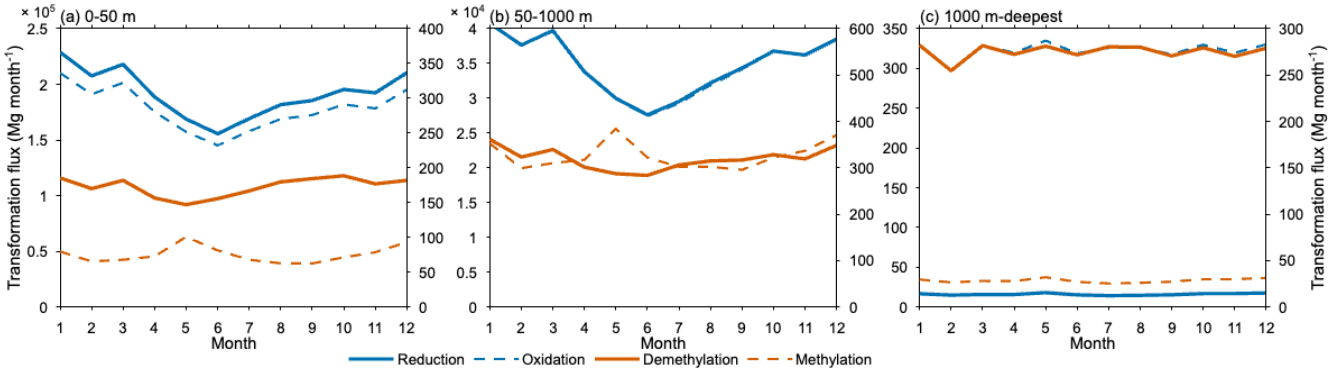


Figure 15. Monthly gross transformation fluxes in different ocean depth layers (0–50, 50–1000, > 1000 m).

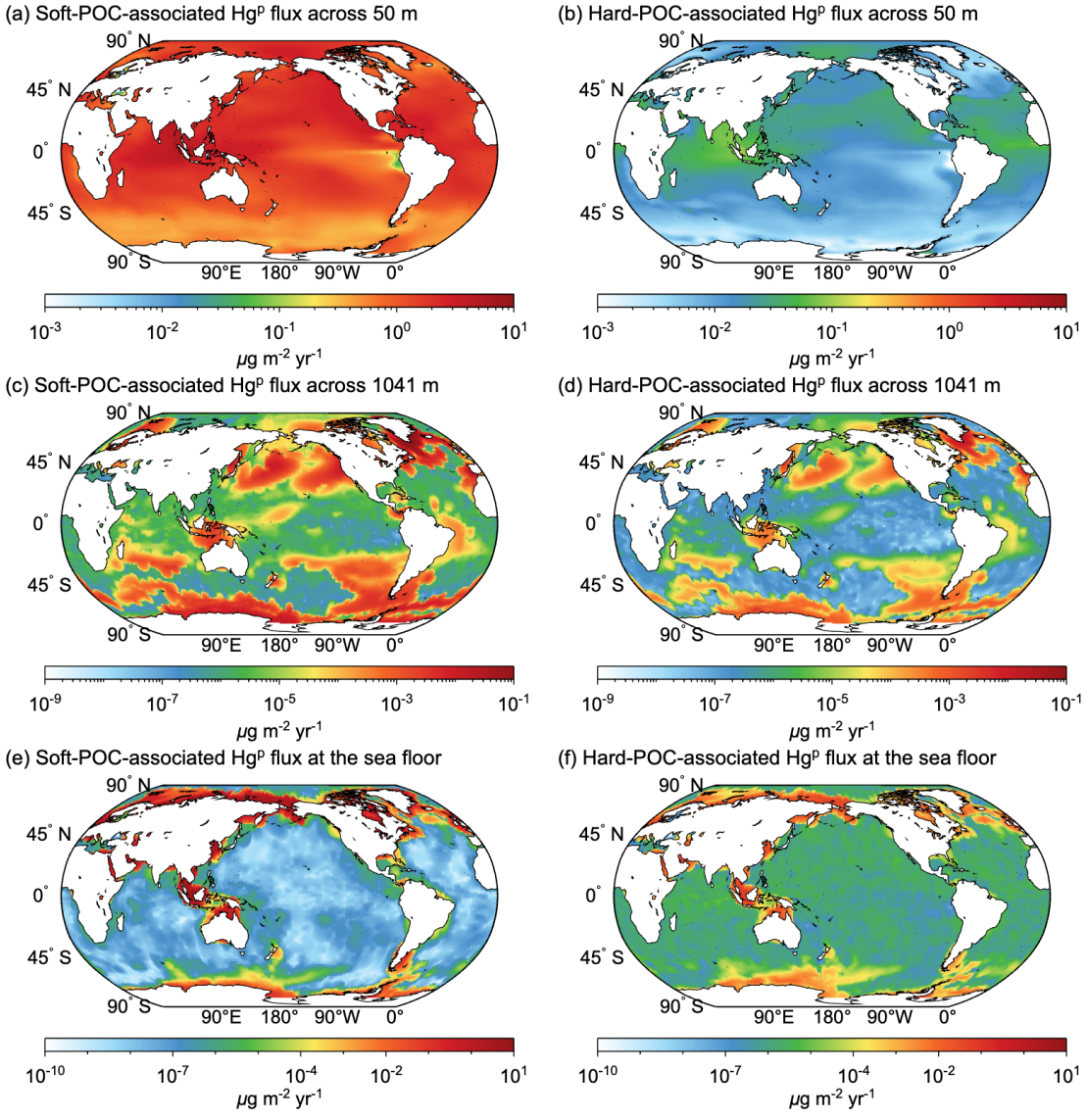


Figure 16. Downward Hg^P fluxes associated with soft POC (left) and hard POC (right) across the 50 m interface **(a–b)**, the 1041 m interface **(c–d)**, and at the seafloor **(e–f)**.

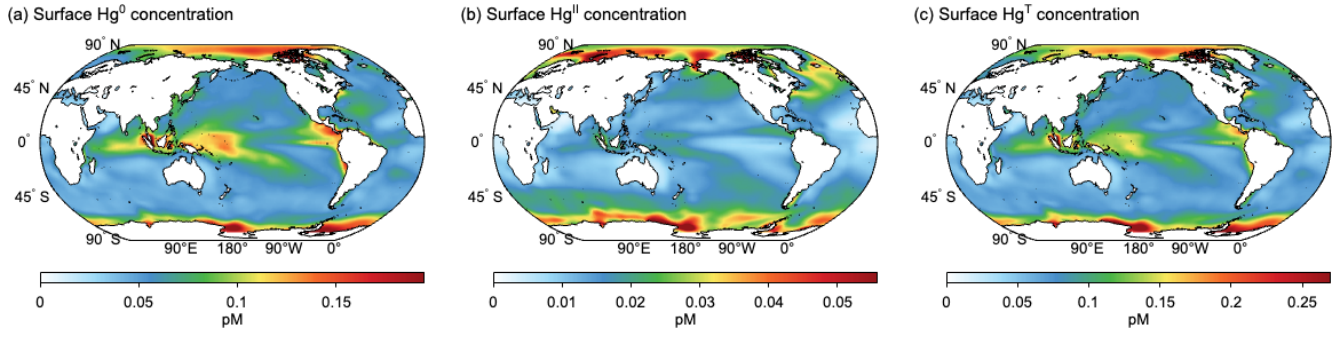


Figure 17. Spatial distributions of **(a)** Hg^0, **(b)** Hg^{II}, and **(c)** Hg^T concentrations at 5 m under the new redox rate settings.

Table 3. Comparison of major Hg biogeochemical diagnostics between the baseline and reduced-redox-rate POP2/Hg simulations.

Budgets ($Mg\ yr^{-1}$)	Baseline	Reduced-rate case
Global net redox budget	1.65×10^5	1.07×10^4
Surface ocean net redox (0–50 m)	1.67×10^5	8.22×10^3
Intermediate ocean net redox (50–1000 m)	1.53×10^3	3.62×10^3
Deep ocean net redox (> 1000 m)	-3.69×10^3	-1.11×10^3
$Hg^{II} \rightarrow$ MMHg methylation	5.16×10^3	8.46×10^2
MMHg $\rightarrow Hg^0$ reductive demethylation	4.86×10^3	4.41×10^3
Hg^0 net evasion	−4432	−4860
DMHg net evasion	−67.48	−35.08
Global Hg inventories (Gg)	360.4	346.4

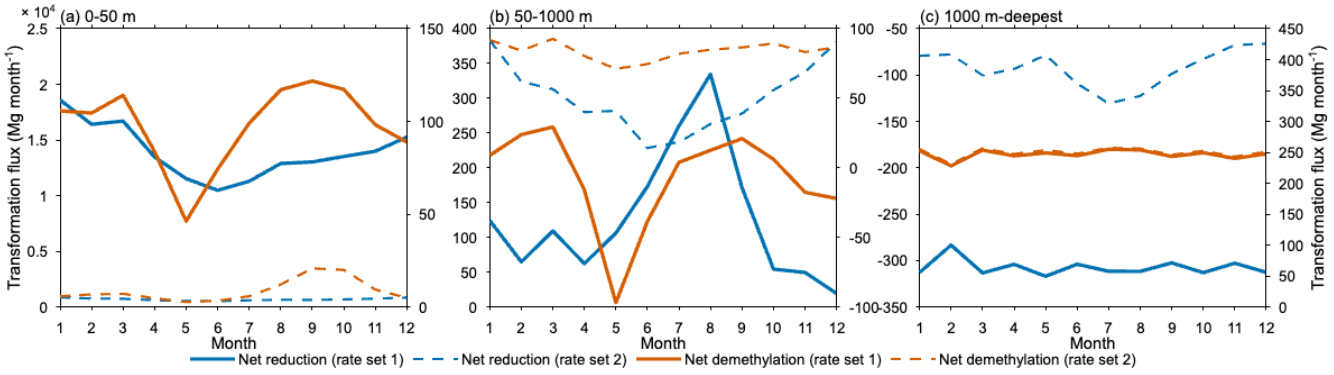


Figure 18. Monthly net transformation fluxes under two chemical rate scenarios, for: 0–50 m (left), 50–1000 m (center), and 1000 m to the deepest ocean layer (right). Set 1 (solid lines): the default reaction rates used in this model; Set 2 (dashed lines): reduced photochemical reaction rates following Bieser et al. (2023).

However, in the deep ocean (> 1000 m), the redox budget remained net oxidizing, but the magnitude of net oxidation decreased from 3.69×10^3 to $1.11 \times 10^3\ Mg\ yr^{-1}$, consistent with the reduced oxidation rates.

The monthly variability of net transformations (Fig. 18) further illustrates this vertical redistribution. In surface waters, the seasonal cycle of net reduction decreases, while demethylation maintains a weak late-summer peak. In the intermediate ocean, the decrease of redox rates increases net reduction, whereas net demethylation changes more modestly. In the deep-ocean, the redox budget remains net oxidizing, but its magnitude is substantially reduced. Methylation and demethylation exhibit weaker seasonal variability than the inorganic redox reactions.

Overall, the sensitivity experiment shows that uncertainty in the prescribed redox rates propagates beyond the direct oxidation and reduction fluxes to upper-ocean Hg speciation, methylation, seasonal variability, and air–sea exchange. The strongest responses occur in the surface ocean, where the changes in Hg0 and HgII concentrations are accompanied by enhanced Hg0 evasion. Comparisons with the currently available observations do not consistently favor either parameter set, identifying the redox-rate parameterization as an important source of uncertainty in the simulated upper-ocean Hg cycle. Further in situ and laboratory measurements under environmentally relevant Hg concentrations are needed to constrain these rates more accurately.

5 Conclusions

We have developed a new global ocean mercury model, POP2/Hg v1.0, by embedding a mercury cycling module into the ocean component POP2 of the CESM2 and coupling it with the Marine Biogeochemistry Library (MARBL). POP2/Hg v1.0 represents an advancement in marine mercury modelling by explicitly simulating redox transformations, air–sea exchange, particle partitioning, and the biologically driven vertical transport of mercury species via soft and hard POC. The model resolves major mercury forms, including Hg^0, Hg^{II}, Hg^P, and methylated mercury species (MMHg and DMHg), and links their behavior to ecosystem dynamics through MARBL's prognostic treatment of soft and hard POC. By integrating microbial methylation in subsurface remineralization zones and allowing for depth-resolved demethylation, the model captures measured MeHg distributions, particularly in oxygen-deficient waters.

The model captures the large-scale spatial patterns of Hg species observed in surface ocean datasets compiled by Zhang et al. (2020). Although the observations span different years and seasons whereas the model fields represent annual means, the collocated surface correlations remain significant, indicating broad spatial consistency despite modest local agreement. Simulation results show that the global Hg^0 net evasion flux is approximately 4.52×10^3 Mg yr^{-1}. Subsurface layers serve as active zones of methylation and demethylation, with annual deep-ocean gross reductive MMHg demethylation of approximately 3.3×10^3 Mg yr^{-1}. Hg^{II} accumulates in intermediate and deep waters due to particle scavenging, with vertical gradients maintained by redox transformations and remineralization dynamics. These results emphasize the importance of the biological pump and microbial processes in shaping the oceanic mercury cycle.

Compared to prior global mercury models such as MITgcm-Hg and MERCY v2.0, POP2/Hg v1.0 offers improved coupling of Hg chemistry with ocean biogeochemistry, dynamic air–sea exchange, and a fully prognostic ecosystem framework. Future model development will focus on a fully coupled CESM2-Hg Earth system model including the atmosphere, land, and ocean, advancing our understanding of mercury behavior in the global ocean and its implications for ecological and human health.

Code and data availability. The POP2/Hg v1.0 model source code (Mao and Zhang, 2025) is archived on Zenodo at https://doi.org/10.5281/zenodo.17766499. The code deposit includes the full POP2/Hg v1.0 implementation, configuration files, and a technical documentation file required to reproduce all simulations presented in this study.

The Hg module is implemented within CESM2.1.3 (UCAR/NCAR, 2020), which is distributed by NCAR under an open-source license. Access to the CESM source code is required to compile and run POP2/Hg v1.0 and is available at https://github.com/ESCOMP/cesm (last access: 2 November 2026).

The forcing and observational datasets used for model evaluation are publicly accessible from the respective data providers as cited in Sect. 2.4. The model output generated in this study is not publicly archived due to file size limitations. However, all simulations can be fully reproduced using the open-source POP2/Hg v1.0 code and the CESM2.1.3 configuration files. Model output is also available from the corresponding author upon reasonable request.

Author contributions. MM developed the POP2/Hg v1.0 model and drafted the manuscript. MM performed the simulations with technical advice from YW and PZ. YZ contributed to model design, interpretation of results, and manuscript revision. LL, SH helped with the collection of data. CZ contributed to supervision and manuscript review.

Competing interests. The contact author has declared that none of the authors has any competing interests.

Disclaimer. Publisher's note: Copernicus Publications remains neutral with regard to jurisdictional claims made in the text, published maps, institutional affiliations, or any other geographical representation in this paper. The authors bear the ultimate responsibility for providing appropriate place names. Views expressed in the text are those of the authors and do not necessarily reflect the views of the publisher.

Acknowledgements. We acknowledge the Louisiana Optical Network Infrastructure (LONI) for providing the high-performance computing resources used in this study. Simulations with CESM2 and POP2/Hg v1.0 were performed on LONI's QB-4 and associated HPC systems, and we thank the LONI staff for their technical support and maintenance of the computational environment.

Financial support. This research has been supported by the National Natural Science Foundation of China (grant no. 42394094).

Review statement. This paper was edited by Paul Halloran and reviewed by three anonymous referees.

References

Bieser, J., Amptmeijer, D. J., Daewel, U., Kuss, J., Soerensen, A. L., and Schrum, C.: The 3D biogeochemical marine mercury cycling model MERCY v2.0 – linking atmospheric Hg to methylmercury in fish, Geosci. Model Dev., 16, 2649–2688, https://doi.org/10.5194/gmd-16-2649-2023, 2023.

Black, F. J., Conaway, C. H., and Flegal, A. R.: Stability of dimethyl mercury in seawater and its conversion to monomethyl mercury, Environ. Sci. Technol., 43, 4056–4062, https://doi.org/10.1021/es9001218, 2009.

Chen, Q., Wu, Q., Cui, Y., and Wang, S.: Global seafood production practices and trade patterns contribute to disparities in exposure to methylmercury, Nat. Food, 6, 491–502, https://doi.org/10.1038/s43016-025-01136-9, 2025.

Dastoor, A., Angot, H., Bieser, J., Brocza, F., Edwards, B., Feinberg, A., Feng, X., Geyman, B., Gournia, C., He, Y., Hedgecock, I. M., Ilyin, I., Kirk, J., Lin, C.-J., Lehnherr, I., Mason, R., McLagan, D., Muntean, M., Rafaj, P., Roy, E. M., Ryjkov, A., Selin, N. E., De Simone, F., Soerensen, A. L., Steenhuisen, F., Travnikov, O., Wang, S., Wang, X., Wilson, S., Wu, R., Wu, Q., Zhang, Y., Zhou, J., Zhu, W., and Zolkos, S.: The Multi-Compartment Hg Modeling and Analysis Project (MCHgMAP): mercury modeling to support international environmental policy, Geosci. Model Dev., 18, 2747–2860, https://doi.org/10.5194/gmd-18-2747-2025, 2025.

Dutay, J. C., Bullister, J. L., Doney, S. C., Orr, J. C., Najjar, R., Caldeira, K., Campin, J.-M., Drange, H., Follows, M., Gao, Y., Gruber, N., Hecht, M. W., Ishida, A., Joos, F., Lindsay, K., Madec, G., Maier-Reimer, E., Marshall, J. C., Matear, R. J., Monfray, P., Mouchet, A., Plattner, G.-K., Sarmiento, J., Schlitzer, R., Slater, R., Totterdell, I. J., Weirig, M.-F., Yamanaka, Y., and Yool, A.: Evaluation of ocean model ventilation with CFC-11: com-

parison of 13 global ocean models, Ocean Model., 4, 89–120, https://doi.org/10.1016/S1463-5003(01)00013-0, 2002.

Kalinchuk, V. V., Lopatnikov, E. A., Astakhov, A. S., Ivanov, M. V., and Hu, L.: Distribution of atmospheric gaseous elemental mercury (Hg(0)) from the Sea of Japan to the Arctic, and Hg(0) evasion fluxes in the Eastern Arctic Seas: Results from a joint Russian-Chinese cruise in fall 2018, Sci. Total Environ., 753, 142003, https://doi.org/10.1016/j.scitotenv.2020.142003, 2021.

Kuss, J., Zülicke, C., Pohl, C., and Schneider, B.: Atlantic mercury emission determined from continuous analysis of the elemental mercury sea-air concentration difference within transects between 50°N and 50°S, Global Biogeochem. Cy., 25, GB3021, https://doi.org/10.1029/2010GB003998, 2011.

Long, M. C., Moore, J. K., Lindsay, K., Levy, M., Doney, S. C., Luo, J. Y., Krumhardt, K. M., Letscher, R. T., Grover, M., and Sylvester, Z. T.: Simulations With the Marine Biogeochemistry Library (MARBL), J. Adv. Model. Earth Sy., 13, e2021MS002647, https://doi.org/10.1029/2021MS002647, 2021.

Mao, M. and Zhang, Y.: CESM2_POP2/Hg_mod, Zenodo [code], https://doi.org/10.5281/zenodo.17766499, 2025.

Mason, R. P., Fitzgerald, W. F., and Morel, F. M. M.: The biogeochemical cycling of elemental mercury: Anthropogenic influences, Geochim. Cosmochim. Ac., 58, 3191–3198, https://doi.org/10.1016/0016-7037(94)90046-9, 1994.

Moore, J. K., Doney, S. C., Kleypas, J. A., Glover, D. M., and Fung, I. Y.: An intermediate complexity marine ecosystem model for the global domain, Deep-Sea Res. Pt. II, 49, 403–462, https://doi.org/10.1016/S0967-0645(01)00108-4, 2001.

Moore, J. K., Doney, S. C., and Lindsay, K.: Upper ocean ecosystem dynamics and iron cycling in a global three-dimensional model, Global Biogeochem. Cy., 18, GB4028, https://doi.org/10.1029/2004GB002220, 2004.

Morel, F. M. M., Kraepiel, A. M. L., and Amyot, M.: The chemical cycle and bioaccumulation of mercury, Annu. Rev. Ecol. Syst., 29, 543–566, https://doi.org/10.1146/annurev.ecolsys.29.1.543, 1998.

Nerentorp Mastromonaco, M. G., Gårdfeldt, K., and Langer, S.: Mercury flux over West Antarctic Seas during winter, spring and summer, Mar. Chem., 193, 44–54, https://doi.org/10.1016/j.marchem.2016.08.005, 2017.

Peng, D., Tan, Z., Yuan, T., Wu, P., Song, Z., Zhang, P., Huang, S., Zhang, Y., Lei, T., Middleton, B. A., Sonke, J. E., Lei, G., and Gao, J.: Human perturbations to mercury in global rivers, Sci. Adv., 11, eadw0471, https://doi.org/10.1126/sciadv.adw0471, 2025.

Smith, R., Jones, P., Briegleb, B. P., Bryan, F. O., Danabasoglu, G., Dennis, J. M., Dukowicz, J., Eden, C., Fox-Kemper, B., Gent, P. R., Hecht, M., Jayne, S., Jochum, M., Large, W. G., Lindsay, K., Maltrud, M., Norton, N. J., Peacock, S. L., Vertenstein, M., and Yeager, S.: The Parallel Ocean Program (POP) Reference Manual: Ocean Component of the Community Climate System Model (CCSM) and Community Earth System Model (CESM), LAUR-10-01853, Los Alamos National Laboratory, Los Alamos, NM, USA, https://files.cesm.ucar.edu/models/pop/2/POPRefManual.pdf (last access: 26 September 2025), 2010.

Soerensen, A. L., Sunderland, E. M., Holmes, C. D., Jacob, D. J., Yantosca, R. M., Skov, H., Christensen, J. H., Strode, S. A., and Mason, R. P.: An Improved Global Model for Air-Sea Exchange of Mercury: High Concentrations over the North Atlantic, Environ. Sci. Technol., 44, 8574–8580, https://doi.org/10.1021/es102032g, 2010.

Soerensen, A. L., Mason, R. P., Balcom, P. H., and Sunderland, E. M.: Drivers of Surface Ocean Mercury Concentrations and Air–Sea Exchange in the West Atlantic Ocean, Environ. Sci. Technol., 47, 7757–7765, https://doi.org/10.1021/es401354q, 2013.

Soerensen, A. L., Mason, R. P., Balcom, P. H., Jacob, D. J., Zhang, Y., Kuss, J., and Sunderland, E. M.: Elemental Mercury Concentrations and Fluxes in the Tropical Atmosphere and Ocean, Environ. Sci. Technol., 48, 11312–11319, https://doi.org/10.1021/es503109p, 2014.

Strode, S., Jaeglé, L., and Emerson, S.: Vertical transport of anthropogenic mercury in the ocean, Global Biogeochem. Cy., 24, GB4014, https://doi.org/10.1029/2009GB003728, 2010.

Sunderland, E. M. and Mason, R. P.: Human impacts on open ocean mercury concentrations, Global Biogeochem. Cy., 21, GB4022, https://doi.org/10.1029/2006GB002876, 2007.

UCAR/NCAR: CESM v2.1.3, GitHub [code], https://github.com/ESCOMP/CESM/tree/release-cesm2.1.3 (last access: 2 November 2026), 2020.

Wang, J., Xie, Z., Wang, F., and Kang, H.: Gaseous elemental mercury in the marine boundary layer and air-sea flux in the Southern Ocean in austral summer, Sci. Total Environ., 603–604, 510–518, https://doi.org/10.1016/j.scitotenv.2017.06.120, 2017.

Wang, Y., Wu, P., and Zhang, Y.: Climate-driven changes of global marine mercury cycles in 2100, P. Natl. Acad. Sci. USA, 120, e2202488120, https://doi.org/10.1073/pnas.2202488120, 2023.

Yuan, T., Zhang, P., Song, Z., Huang, S., Wang, X., and Zhang, Y.: Buffering effect of global vegetation on the air-land exchange of mercury: Insights from a novel terrestrial mercury model based on CESM2-CLM5, Environ. Int., 174, 107904, https://doi.org/10.1016/j.envint.2023.107904, 2023.

Zhang, P. and Zhang, Y.: Earth system modeling of mercury using CESM2 – Part 1: Atmospheric model CAM6-Chem/Hg v1.0, Geosci. Model Dev., 15, 3587–3601, https://doi.org/10.5194/gmd-15-3587-2022, 2022.

Zhang, Y., Jaeglé, L., and Thompson, L.: Natural biogeochemical cycle of mercury in a global three-dimensional ocean tracer model, Global Biogeochem. Cy., 28, 553–570, https://doi.org/10.1002/2014GB004814, 2014a.

Zhang, Y., Jaeglé, L., Thompson, L., and Streets, D. G.: Six centuries of changing oceanic mercury, Global Biogeochem. Cy., 28, 1251–1261, https://doi.org/10.1002/2014GB004939, 2014b.

Zhang, Y., Soerensen, A. L., Schartup, A. T., and Sunderland, E. M.: A Global Model for Methylmercury Formation and Uptake at the Base of Marine Food Webs, Global Biogeochem. Cy., 34, e2019GB006348, https://doi.org/10.1029/2019GB006348, 2020.

Zhang, Y., Song, Z., Huang, S., Zhang, P., Peng, Y., Wu, P., Gu, J., Dutkiewicz, S., Zhang, H., Wu, S., Wang, F., Chen, L., Wang, S., and Li, P.: Global health effects of future atmospheric mercury emissions, Nat. Commun., 12, 3035, https://doi.org/10.1038/s41467-021-23391-7, 2021.